High-Resolution Microwave Images of Saturn

A. W. Grossman, D. O. Muhleman, G. L. Berge

An analysis of high-resolution microwave images of Saturn and Saturn's individual rings is presented. Radio interferometric observations of Saturn taken at the Very Large Array in New Mexico at wavelengths of 2 and 6 centimeters reveal interesting new features in both the atmosphere and rings. The resulting maps show an increase in brightness temperature of about 3 K from equator to pole at both wavelengths, while the 6-centimeter map shows a bright band at northern mid-latitudes. The data are consistent with a radiative transfer model of the atmosphere that constrains the well-mixed, fully saturated, NH_3 mixing ratio to be 1.2×10^{-4} in a region just below the NH_3 clouds, while the observed bright band indicates a 25 percent relative decrease of NH_3 in northern mid-latitudes. Brightness temperatures for the classical rings are presented. Ring brightness shows a variation with azimuth and is linearly polarized at an average value of about 5 percent. The variations in ring polarization suggest that at least 20 percent of the ring brightness is the result of a single scattering process.

Microwave observations provide a direct means of sensing the deep atmosphere of Saturn and probing the rings of Saturn at a wavelength comparable to individual ring particle sizes. Recent Very Large Array (VLA) observations of Saturn and Saturn's rings have sufficient spatial resolution and sensitivity to detect small-scale brightness variations in both the atmosphere and the rings (*1*). Previous microwave interferometer observations have been limited in spatial resolution and sensitivity, which restricts the usefulness of the data to fitting global brightness models to the disk and rings (*2–4*). We improve on earlier VLA results by using more telescopes, thereby producing unambiguous microwave maps of the Saturn system and separating the contribution to the total brightness from the disk and individual ring systems. We directly measure latitudinal brightness variations on the disk, azimuthal brightness variations and polarization in the rings, and attenuation of the disk brightness by the rings.

We examine the observed atmospheric brightness variations by developing a radiative transfer model for Saturn's atmosphere and by showing that the observed variations are largely due to two effects: variations in NH_3 abundance and temperature profile. Because NH_3 is the major source of opacity, we can show that the data are consistent with a model of Saturn's atmosphere in which both NH_3 and temperature vary with latitude. In addition to showing latitudinal brightness variations in the atmosphere, the high-resolution maps reveal azimuthal variations in ring brightness. Previous observations have shown that ring particles scatter the thermal emission of Saturn to Earth and emit little thermal emission of their own at centimeter wavelengths (*4*). Thus the azimuthal variations in ring brightness measure the scattering phase function of the rings. Finally we present observations of polarized ring brightness and relate these to the scattering properties of Saturn's rings.

Observations and data reduction. We observed Saturn for 2 days at two wavelength bands using a 50-Mhz bandwidth at two adjacent frequencies. Table 1 summarizes the observational parameters of the experiment. The data were scaled and rotated to a common reference before summing to produce one map at each wavelength of 2 and 6 cm. Owing to the length of the observing period relative to the rotation rate of Saturn, longitudinal information is smeared in time and only latitudinal variations are observable. Radio sources 1519 − 273 and 1657 − 261, which were close to Saturn, were used to calibrate phases. Radio source 3C286 served as our primary reference calibrator in amplitude and polarization and is accurate to within 3% on an absolute flux scale established by Baars *et al.* (*5*).

The sensitivity in the maps is limited by noise caused by short time-scale terrestrial atmospheric fluctuations and turbulence. We are able to reduce this source of noise by applying a technique commonly known as self-calibration, which makes use of some a

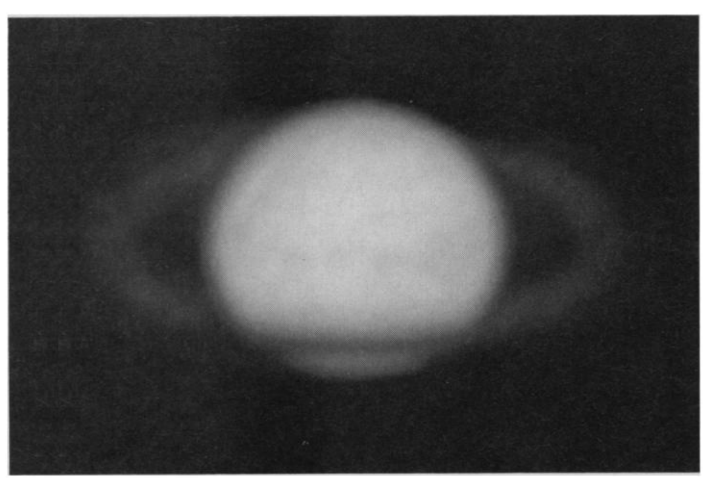

Fig. 1. Brightness map of Saturn at a wavelength of 2 cm. The image contrast has been stretched in order to flatten the histogram and enhance low-contrast features on the planetary disk and low-brightness features in the rings.

The authors are in the Division of Geological and Planetary Sciences, California Institute of Technology, Pasadena, CA 91125.

Table 1. Observation log. Saturn and Saturn's rings were observed at wavelengths of 2 and 6 cm over the course of 4 days during 1986. Integration time represents the total time spent observing Saturn. The duration of the experiment is longer. Data at each wavelength were rotated and scaled to a common reference before adding to produce one map at each wavelength.

Observation date	λ (cm)	Frequency (GHz)	Integration (hours)	Distance (AU)	Ring* angle	Map resolution	
						Arc sec	R_s†
22 June 1986	6.17	4.835, 4.885	5.8	9.069	25.11°	1.2	0.131
24 June 1986	6.17	4.835, 4.885	5.6	9.084	25.10°		
14 July 1986	2.01	14.915, 14.965	4.6	9.286	25.03°	1.2	0.151
30 September 1986	2.01	14.915, 14.965	4.4	10.488	25.55°		

*Saturnicentric latitude of the earth. †R_s = 60,268 km (equatorial radius).

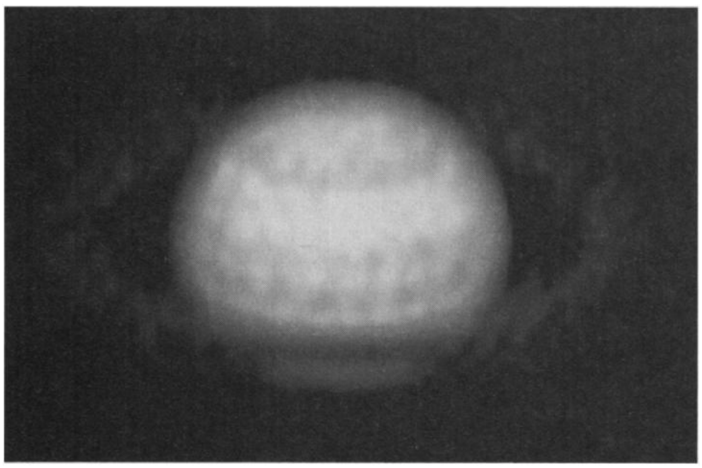

Fig. 2. Brightness map of Saturn at a wavelength of 6 cm. The image contrast has been stretched in order to flatten the histogram and enhance low-contrast features on the planetary disk and low-brightness features in the rings.

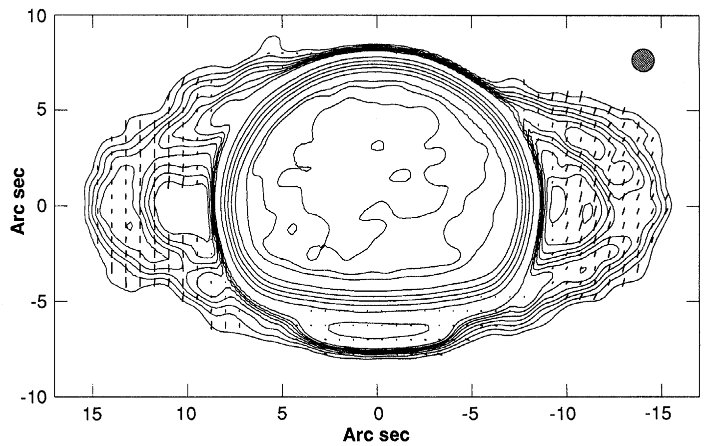

Fig. 3. Brightness contours and polarization vectors at a wavelength of 2 cm. Contours at 2, 3, 4, 5, 6, 7, 8, 10, 30, 50, 70, 90, 110, 130, 134, and 138 K before 2.7 K correction for microwave background. Average polarization vector is 5%, and maximum polarization is 19%. The filled circle represents the 1.2–arc sec resolution of the beam.

priori knowledge of the source brightness distribution (*6*).

The resulting data set of visibilities, which is obtained for all four Stokes parameters, is the spatial Fourier transform of the source intensity distribution. The observed visibility coverage, however, is incomplete, and the direct Fourier transform produces a "dirty map" of the source intensity which represents the true intensity convolved with the synthesized beam pattern. Deconvolution of the total intensity was performed by applying the CLEAN procedure (*7*).

The resulting brightness maps of the total intensity at 2 and 6 cm are shown in Figs. 1 and 2. The root-mean-square uncertainty of any single pixel in the maps is ±0.5 K at 2 cm and ±1.2 K at 6 cm. Maps of linear polarized intensity (*8*), which are near the signal-to-noise threshold of the VLA, cannot be deconvolved by the CLEAN algorithm. Figures 3 and 4 show Saturn radio brightness contour maps at 2 and 6 cm as well as superimposed linear polarization vectors that indicate the percent magnitude and direction of polarized intensity.

Brightness temperature of disk and rings. The ring is clearly visible on either side of the disk of Saturn as well as in a cusp, due to extinction, in front of the southern hemisphere of the planet. For comparison with other observations, and in order to determine ring optical depths, we can directly fit the brightness maps to models of constant intensity for nine regions on Saturn: the planetary disk, four rings, and four cusps (where the rings cross the disk). The results of the linear least-squares estimation are shown in Table 2 along with standard errors based on the goodness of the fit. Systematic errors in the absolute flux, which are believed to be less than 5%, are not included. Whole disk brightness temperatures of 140.4 K at 2.01 cm and 176.7 K at 6.17 cm agree with previous observations at similar wavelengths (*3*).

In determining the brightness temperature of the atmosphere we have corrected for the contrast between the atmosphere and the microwave background by adding 2.7 K to the measured atmospheric brightness temperature. Such a correction factor is not necessary for the rings, which are conservative scatters and, unlike the atmosphere, scatter the microwave background radiation into the beam of the telescope.

Vectors in Figs. 3 and 4 indicate the percent magnitude and direction of linearly polarized intensity. The vectors show an intensity component on the rings that is linearly polarized in a direction perpendicular to the plane of scattering and increases toward the ring ansae. The average polarized brightness is 5% ± 1% of the total ring brightness at both wavelengths while the peak is about 19% at 2 cm and 20% at 6 cm.

The 6-cm maps of Figs. 2 and 4 reveal a band of increased brightness in northern mid-latitudes, in contrast to Figs. 1 and 3 which show no such variation at 2 cm. The high-resolution maps can be used to extract variations in brightness as a function of latitude. Figure 5 shows the variation of atmosphere brightness as a function of planetographic latitude at both wavelengths for a region within one beam width of the sub-earth meridian. A hot band extends from about +20° to +50° in the 6-cm data. This warm band is not visible in the 2-cm data. In addition, a slight equator-to-pole warming is observed at both wavelengths in Fig. 5.

Atmospheric model. The brightness of Saturn and the hot band at northern mid-latitudes can best be understood by comparing

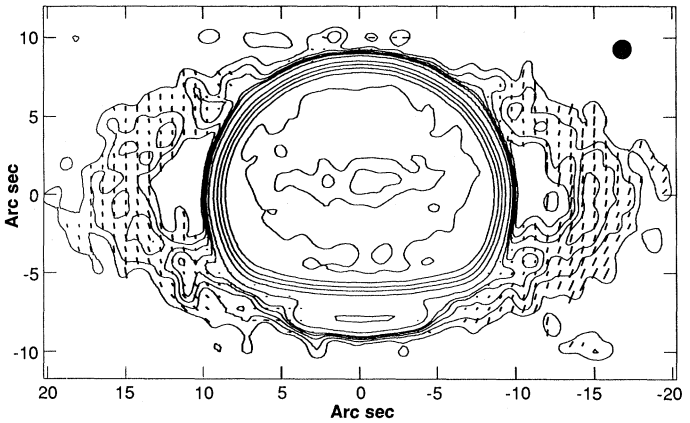

Fig. 4. Brightness contours and polarization vectors at a wavelength of 6 cm. Contours at 3, 5, 7, 9, 11, 20, 50, 80, 110, 140, 170, 180, and 185 K before 2.7 K correction for microwave background. Average polarization vector is 5%, and maximum polarization is 20%. The filled circle represents the 1.2–arc sec resolution of the beam.

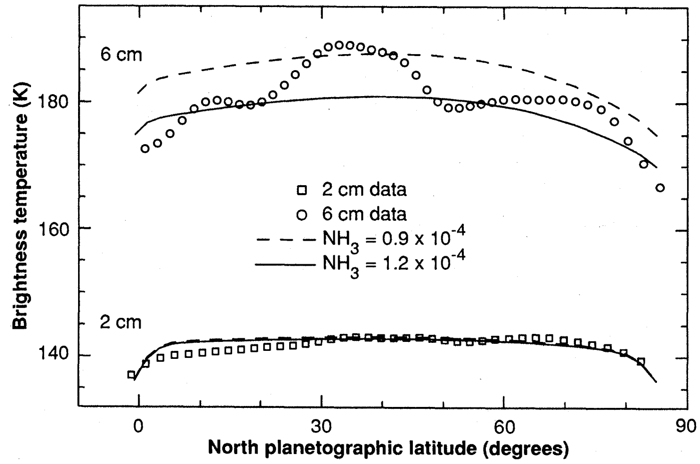

Fig. 5. Brightness temperature as a function of latitude for data at both wavelengths, as well as two models at each wavelength. Root-mean-square uncertainties of the data are 0.5 K at 2 cm and 1.2 K at 6 cm. The models are based on uniformly mixed, fully saturated NH_3 and differ only in their NH_3 mixing ratio below the cloud deck. The change produces little difference at 2 cm but can explain the variation in 6-cm brightness. Both data sets exhibit an equator-to-pole increase in brightness that is not predicted by the model.

observations with theoretical radiative transfer models of the atmosphere (*3, 9*). The brightness temperature, T_B, at a fixed wavelength of an observed region in the atmosphere with direction cosine μ relative to the local normal is

$$T_B(\mu) = \int_0^\infty T(\tau)e^{(-\tau/\mu)}d\tau/\mu \qquad (1)$$

in the Rayleigh-Jeans limit, where the normal optical depth $\tau(z)$ at a height z in the atmosphere is

$$\tau(z) = \int_z^\infty \alpha(z')dz' \qquad (2)$$

and $\alpha(z')$ is the absorption coefficient at height z' at the observational wavelength. Our model calculations integrate Eq. 1 subject to constraints on atmospheric composition, atmospheric temperature profile, and microwave absorption coefficient.

The model atmosphere consists of H_2, He, CH_4, and NH_3. The H_2, He, and CH_4 are uniformly mixed throughout the atmosphere with molar mixing ratios of 0.963, 0.033, and 0.004 (*10*). We assume NH_3 to be saturated in the upper atmosphere (*11*), and we adjust its uniform mixing ratio in the lower atmosphere to agree with our observations. The temperature-pressure profile in the upper atmosphere is obtained from Voyager radio occultation data (*11*). A wet adiabatic gradient is used to extrapolate to greater depths. In the absence of condensibles, a dry adiabat is used.

The model microwave absorption coefficient includes three major sources of opacity: NH_3 inversion bands, NH_3 rotation bands, and H_2 collision-induced dipole rotation bands (*12*). Other potential sources of opacity such as collision-induced dipole CH_4, clouds of H_2O and NH_3, ionosphere, and thermal ionization deep in the atmosphere are negligible. The primary sources of opacity in the atmosphere are the inversion bands of NH_3 centered near 1.3 cm. The Ben Reuven absorption profile has successfully been used to model the pressure-broadened NH_3 lines of the giant planets, and we use it in our model as well (*3, 13*).

The details of the atmospheric model are illustrated in Fig. 6, which shows the temperature profile, NH_3 abundance, and weighting functions at both wavelengths. We compute the brightness of each point on the model image by integrating Eq. 1 along ellipsoidal shells of the atmosphere carefully accounting for the variation of gravity with latitude. The resulting model image is convolved by a gaussian comparable to the gaussian beam shape in the data maps. We tested the model brightness for sensitivity to variations in the

Table 2. Whole-disk and ring model fit results. A model consisting of nine regions of constant flux was fit to the data maps by means of a least-squares technique. Standard errors of the values are given. Systematic errors are less than 5%. The disk brightness applies only to the Northern hemisphere since the Southern hemisphere is largely occulted by the rings. Large errors on the A cusp and Cd cusp are due to the large ring opening angle and limited area occulted by these regions.

Component	Brightness temperature (K)	
	2 cm	6 cm
Disk	140.4 ± 0.4	176.7 ± 0.4
A ring	3.9 ± 0.8	4.3 ± 0.9
Cd ring	0.0 ± 2.7	0.5 ± 2.7
B ring	7.6 ± 0.6	7.7 ± 0.7
C ring	3.0 ± 0.9	2.8 ± 1.0
A cusp	20.3 ± 12.5	59.2 ± 11.3
Cd cusp	92.6 ± 15.1	102.9 ± 14.0
B cusp	14.8 ± 2.0	21.0 ± 2.0
C cusp	99.9 ± 1.9	154.9 ± 2.0

abundance of He, CH_4, H_2O, and ortho-para hydrogen ratios. In all cases, the model is insensitive to variations in these parameters and is dominated by the NH_3 abundance and temperature profile. Indeed, the greatest uncertainty in the model is attributable to the estimate of the NH_3 absorption coefficient at pressures and temperatures applicable to Saturn.

The data at both wavelengths are consistent with a model that contains a uniform NH_3 global mixing ratio of $1.2^{+0.6}_{-0.4} \times 10^{-4}$, where we have only included the 5% uncertainty in the absolute calibration of the data. Recent laboratory measurements that claim that the Ben Reuven absorption profile may be too great by as much as 40% (*14*) may change our absolute determination of NH_3 abundance, but do not fundamentally change our conclusions, which rely on relative variations in NH_3.

Figure 5 shows the results of the model calculations for two concentrations of NH_3 superimposed on the observational data. The two different concentrations of NH_3 produce distinct variations in brightness at 6 cm, however, the two curves at 2 cm are indistinguishable. This can best be understood by considering the weighting functions of Fig. 6, which illustrate that observations at 2 cm, near the center of the NH_3 band, are most sensitive to the temperature just above the saturation point, while observations at 6 cm probe below the NH_3 saturation point. As a result, the 2-cm data appear to be consistent with fully saturated NH_3 and are not sensitive to variations in NH_3 abundance below the saturation point. In fact, the good agreement between the model and data at 2 cm serves as an independent test of the Baars *et al.* absolute flux scale (*5*). On the other hand, the 6-cm data are most sensitive to variations in NH_3 below the saturation point. Thus variations in brightness observed at 6 cm and not at 2 cm must be directly related to variations in NH_3 abundance, while brightness variations observed at both wavelengths are the result of changes in kinetic temperature. In this respect, the bright zone at northern mid-latitudes is a region of NH_3 depletion, relative to the global distribution. In the context of our model, this corresponds to a 25% decrease in the NH_3 mixing ratio to a value of 0.9×10^{-4}.

The data do not rule out the possibility that the hot band is caused by a meridional temperature variation of 8 K at deep levels. However, the difficulties of sustaining a large temperature deviation in the presence of convection argues against this explanation. Furthermore, Voyager spacecraft observations support the conclusion that the hot band at northern mid-latitudes is a region of decreased opacity. Inversion of infrared spectra shows a region of increased brightness at a level of 0.73 bar in northern mid-latitudes

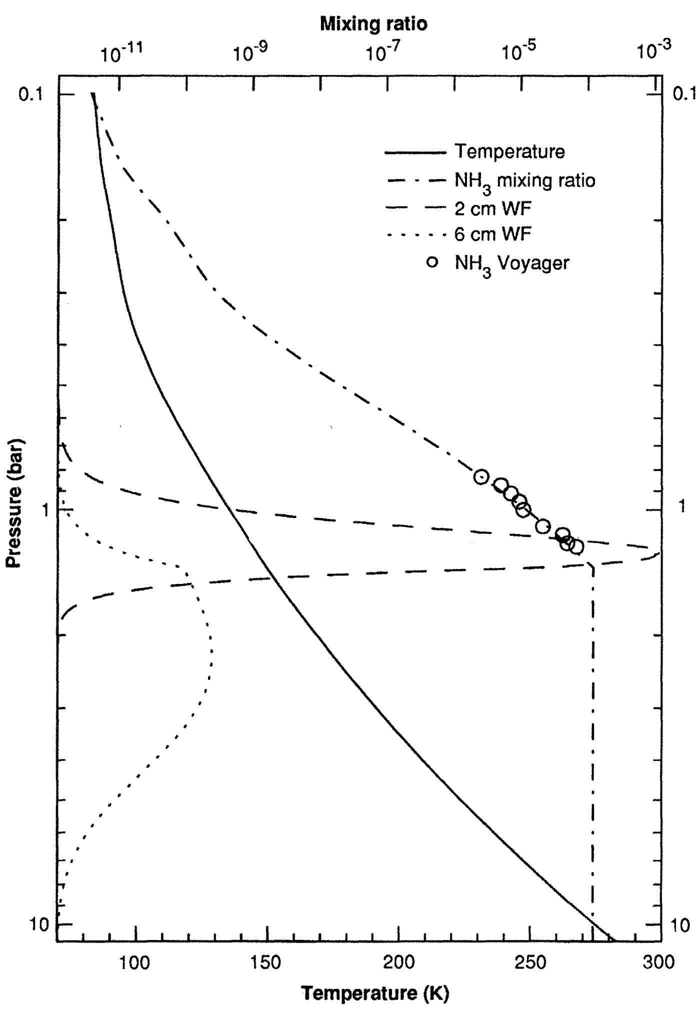

Fig. 6. Vertical profile of the model atmosphere. Solid line is the temperature profile extrapolation with a wet adiabat. Other lines include NH_3 mixing ratio and normalized weighting functions (WF) at 2 cm and 6 cm. Circles are the NH_3 saturation abundance as measured by the Voyager Radio Occultation experiment (*11*).

Table 3. Normal ring optical depths and differential optical depths. These values are derived from Table 2 and the assumption of a many-particle-thick ring layer. Standard errors of the values are given. The large optical depths may be systematically underestimated by as much as 5%. The meaningless negative differential optical depth of the Cassini Division (Cd) has not been included.

Component	τ[2.01 cm]	τ[6.17 cm]	$\Delta\tau$*/τ[2.01 cm]
A ring	0.91 ± 0.33	0.49 ± 0.09	0.46
Cd ring	0.17 ± 0.07	0.23 ± 0.06	—
B ring	1.26 ± 0.12	1.10 ± 0.07	0.13
C ring	0.15 ± 0.01	0.06 ± 0.01	0.62

*$\Delta\tau = \tau[2.01\text{ cm}] - \tau[6.17\text{ cm}]$.

(*15*) that is surprisingly similar in shape and position to the hot band observed at 6 cm. The infrared measurements suggest that the far infrared particulate opacity must be a minimum at these latitudes (*16*). One possible explanation for the similarity is that the same vertical motions that reduce infrared opacity at 0.73 bar extend deep into the atmosphere and are responsible for NH_3 clearing below the clouds.

Both wavelengths exhibit a similar 3 K increase in brightness relative to the model from equator to pole. The equator-to-pole brightening is most convincing at 2 cm, a wavelength that is most sensitive to the temperature at the NH_3 condensation point. This brightness increase is most likely caused by an increase in kinetic temperature along constant pressure surfaces. The strong similarity of the equator-to-pole temperature increase at the two wavelengths argues against an explanation involving NH_3 absorption alone.

One possible mechanism for producing a meridional temperature gradient may be the latitudinal variation of ortho-para hydrogen. The heat released in conversion from ortho to para H_2 has been estimated to be on the order of 5 K (*17*), which is consistent with the observed temperature increase.

Ring model. Radiation from the rings arises because of three distinguishable physical processes: intrinsic thermal emission (which is negligible at our wavelength), emission from the planetary disk of Saturn (which is subsequently scattered by the ring particles), and, for the region of the rings that occults the disk, emission from the planetary disk attenuated by the rings.

The gross structure of the rings can be understood by examining the normal optical depth of the rings. Previous microwave observations have determined the normal optical depth, τ, at various ring opening angles (*2*), and we expand on this knowledge by determining τ at a ring opening angle of $B \sim 25°$.

The brightness temperature of the cusp T_C is given by the sum of attenuated planetary disk brightness T_D and the intrinsic ring brightness in front of the cusp T_R:

$$T_C = T_D \exp(-\tau/\sin|B|) + T_R \quad (3)$$

where B is the ring opening angle. We insert the data of Table 2 into Eq. 3 and solve for τ to generate the results in Table 3, which also shows the normalized optical depth $\Delta\tau/\tau$[2.01 cm], where $\Delta\tau = \tau[2.01\text{ cm}] - \tau[6.17\text{ cm}]$.

The greatest source of bias in deriving the normal optical depth from Eq. 3 lies in estimating the intrinsic brightness of the ring at the cusp, T_R, from its value at the ring ansae. These results assume that the intrinsic ring brightness at the cusp is equal to a constant flux model that is fit to regions at the ring ansae. The data, however, show a slightly increased brightness toward the cusp. As a result, estimates of T_R used in Eq. 3 and derived from Table 2 are low and the resulting optical depths in Table 3 are probably low as well. The bias is clearly the greatest for the larger optical depths, but in no case is it larger than 5%.

The extinction of the disk brightness is primarily the result of conservative scattering by the ring particles. The normal optical depth, as defined by Eq. 3, is a measure of the second moment of the particle size distribution for those particles with radius $a \gtrsim \lambda/\pi$ and is directly comparable to the optical depth derived in occultation experiments with natural sources (*18*). With this approximation, the fraction $\Delta\tau/\tau$[2.01 cm] is roughly the fractional projected area of particles in the size range 0.6 to 2.0 cm (*19*). Table 3 can thus be interpreted as indicating that the A and C rings contain many particles in this size range while the B ring contains a greater population of large particles. In contrast, the Cassini Division appears to be lacking in centimeter size particles. The similarity of the 2-cm optical depths to those obtained at ultraviolet and visible wavelengths by the Voyager spacecraft (*20*) supports the conclusion that few particles are smaller than 0.6 cm. This finding confirms the results of the Voyager Radio Occultation for the A ring, C ring, and Cassini Division (*21*) and extends the results to the B ring.

Azimuthal variations in ring brightness can be related to the ensemble scattering phase function of the ring particles. Current high-resolution observations can be used to test the existing theoretical models of ring scattering behavior (*4*). The models suggest that the ring should appear brightest at forward scattering angles, in front of the planet, and decrease in brightness at larger scattering angles. This simple model agrees with the 6-cm map, which shows an increased brightening in the forward direction; however, the 2-cm map shows no such variation with azimuth and suggests a need for more detailed modeling. One prediction of the models is observed in the data: the C ring appears nearly as bright as the A ring despite the low optical depth of the C ring. This is simply the result of Saturn subtending a much larger angle as seen from the C ring than as seen from the A ring.

No current model, however, considers the polarization of the scattered radiation from Saturn's rings. Figures 3 and 4 show that the total polarized flux has an average amplitude of 5% ± 1% and is generally oriented perpendicular to the mean scattering plane. Peak polarized flux reaches values of 20% at the ansae. The production of polarized radiation from the scattering of unpolarized radiation is generally a result of single scattering and suggests that at least 20% of the scattered emission is the result of a single scattering process.

The linear polarization is suggestive of Rayleigh scattering but the wavelength independence of the polarized flux and the low scattering efficiency rules out such a model. The polarized flux is most likely due to Fresnel reflection, which is highly polarized perpendicular to the scattering plane (*22*). Additional modeling is required to understand this phenomenon.

Future prospects. Despite these high-resolution observations of Saturn, much remains to be learned about both the atmosphere and the rings. Observations at additional wavelengths penetrate the atmosphere to different depths and may further constrain NH_3 abundance and distribution as well as confirm the existence of other sources of microwave opacity. Ring brightness and optical depths obtained at different ring opening angles may be used to constrain the ring particle size distribution. Additional electromagnetic scattering models need to be developed in order to understand current observations.

The observations presented in this article represent the ultimate in resolution and sensitivity obtainable from Earth-based radio telescopes. A vast improvement in our knowledge of Saturn's deep atmosphere and rings can be obtained from a Saturn-orbiting spacecraft instrument observing at radio wavelengths.

REFERENCES AND NOTES

1. Observations were first reported in A. W. Grossman, D. O. Muhleman, G. L. Berge, *Bull. Amer. Astron. Soc.* **20**, 880 (1988); *ibid.* **19**, 848 (1987). The design and performance of the National Radio Astronomy Observatory Very Large Array is fully discussed in P. J. Napier, A. R. Thompson, and R. D. Ekers [*Proc. IEEE* **71–11**, 1295 (1983)]. The National Radio Astronomy Observatory is operated by Associated Universities, Inc., under contract with the National Science Foundation.
2. T. E. Dowling, D. O. Muhleman, G. L. Berge, *Icarus* **70**, 506 (1987); I. De Pater and J. R. Dickel, *ibid.* **50**, 88 (1982); F. P. Schloerb, D. O. Muhleman, G. L. Berge, *ibid.* **42**, 125 (1980); J. N. Cuzzi and W. A. Dent, *Astrophys. J.* **198**, 223 (1975).
3. I. De Pater and S. T. Massie, *Icarus* **62**, 143 (1985); M. J. Klein, M. A. Janssen, S. Gulkis, E. T. Olsen, in *The Saturn System, NASA Conference Publication 2068*, D. M. Hunten and D. Morrison, Eds. (NASA, Washington, DC, 1978), pp. 195–216.
4. D. O. Muhleman and G. L. Berge, in *Proceedings of the I.A.U. Colloquium 75, Planetary Rings*, A. Brahic, Ed. (Cepadues-Editions, Toulouse, France, 1984), pp. 57–70; J. N. Cuzzi, J. B. Pollack, A. L. Summers, *Icarus* **44**, 683 (1980); F. P. Schloerb, D. O. Muhleman, G. L. Berge, *ibid.* **39**, 214 (1979); J. N. Cuzzi and D. Van Blerkom, *ibid.* **22**, 149 (1974).
5. J. W. M. Baars, R. Genzel, I. I. K. Pauliny-Toth, A. Witzel, *Astron. Astrophys.* **61**, 99 (1977).
6. The technique of self-calibration makes use of the fact that most of the errors are associated with individual antennas rather than baselines, and it is possible to form a combination of the measured visibilities that is independent of such errors. In the case of Saturn, the phases of the 27 complex antenna gains were fit to the 351 observed data points by means of a simple model of elliptical source brightness. The resulting data were then used to produce a better map of source intensity which served as input to the next iteration of antenna gain solution. A thorough explanation of the procedure can be found in T. J. Pearson and A. C. S. Readhead [*Ann. Rev. Astron. Astrophys.* **22**, 97 (1984)].
7. CLEAN deconvolves the synthetic beam pattern from the "dirty" map by iteratively subtracting a fraction of the interferometer response from the brightest point in the remaining map. The resulting set of clean components is then added back into the map and a gaussian beam equivalent to that of a filled aperture of the same size as the VLA is convolved with the final image. CLEANing of the map departed from the conventional procedure in that we started with an initial model consisting of an ellipse of constant flux. A detailed description of the algorithm is presented by T. Cornwell [in *Synthesis Imaging: Course Notes from an NRAO Summer School*, R. A. Perley, F. R. Schwab, A. H. Bridle, Eds. (National Radio Astronomy Observatory, Green Bank, WV, 1985), pp. 109–121].
8. A partially linearly polarized wave can be represented by the Stokes parameters I, Q, and U, where I is the total intensity of the radiation field, and Q and U describe the linear polarization. Linear polarized intensity is then defined as $(Q^2 + U^2)^{1/2}$, while percentage linear polarized intensity is given by $100(Q^2 + U^2)^{1/2}/I$. The direction of linear polarization is given by the angle Ψ with respect to north and defined in terms of the Stokes parameters by the equation $\tan 2\Psi = U/Q$.
9. G. T. Wrixon and W. J. Welch, *Icarus* **13**, 163 (1970).
10. B. J. Conrath, D. Gautier, R. A. Hanel, J. S. Hornstein, *Astrophys. J.* **282**, 807 (1984).
11. G. F. Lindal, D. N. Sweetnam, V. R. Eshleman, *Astron. J.* **90**, 1136 (1985).
12. G. L. Berge and S. Gulkis, in *Jupiter*, T. Gehrels, Ed. (Univ. of Arizona Press, Tucson, 1976), pp. 621–692.
13. P. G. Steffes and J. M. Jenkins, *Icarus* **72**, 35 (1987).
14. T. R. Spilker and V. R. Eshleman, *Bull. Amer. Astron. Soc.* **20**, 867 (1988). These laboratory measurements were made at temperatures above 210 K and may not be directly applicable to Saturn.
15. B. J. Conrath and J. A. Pirraglia, *Icarus* **53**, 286 (1983).
16. A. P. Ingersoll, R. F. Beebe, B. J. Conrath, G. E. Hunt, in *Saturn*, T. Gehrels and M. S. Matthews, Eds. (Univ. of Arizona Press, Tucson, 1984), pp. 195–238.
17. S. T. Massie and D. M. Hunten, *Icarus* **49**, 213 (1982).
18. Generally speaking, an experiment that observes the occultation of a natural source by Saturn's rings detects both the transmitted wave, which is reduced in amplitude, as well as the primary diffraction lobe of the scattered wave. An experiment that is able to separate these two waves, such as the Voyager radio occultation experiment, reports an optical depth that is twice as great, since the diffraction lobe accounts for half the extinction. This has been discussed more fully by J. N. Cuzzi and J. B. Pollack [*Icarus* **33**, 233 (1978)].
19. G. L. Tyler, E. A. Marouf, R. A. Simpson, H. A. Zebker, V. R. Eshleman, *ibid.* **54**, 160 (1983).
20. J. N. Cuzzi *et al.*, in *Planetary Rings*, R. Greenberg and A. Brahic, Eds. (Univ. of Arizona Press, Tucson, 1984), pp. 73–199.
21. H. A. Zebker, E. A. Marouf, G. L. Tyler, *Icarus* **64**, 531 (1985); E. A. Marouf, G. L. Tyler, H. A. Zebker, R. A. Simpson, V. R. Eshleman, *ibid.* **54**, 189 (1983).
22. K. L. Liou and J. E. Hansen, *J. Atmos. Sci.* **28**, 995 (1971); J. E. Hansen, *ibid.*, p. 1400.

23. We thank the scientists and staff of the VLA for their support. This is contribution number 4753 of the Division of Geological and Planetary Sciences, California Institute of Technology. This research was supported in part by NSF grant ATS8601111 and NASA grant NAGW 1448.

24 May 1989; accepted 25 July 1989